

Synthesis of Single-Crystalline LiMn_2O_4 with Different Dimensional Nanostructures for Li-ion Batteries

Yige Sun^{1,2}, Chengjun Xu¹, Baohua Li^{1,*}, Jinzao Xu¹, Yanbing He¹, Hongda Du¹, Feiyu Kang^{1,2,*}

¹ Key Laboratory of Thermal Management Engineering and Materials, Engineering Laboratory for Functionalized Carbon Materials, Graduate School at Shenzhen, Tsinghua University, Shenzhen, Guangdong Province, 518055, P. R. China.

² State Key Laboratory of New Ceramics and Fine Processing, Department of Materials Science and Engineering, Tsinghua University, Beijing 100084, China

*E-mail: libh@mail.sz.tsinghua.edu.cn; fykang@mail.tsinghua.edu.cn

Received: 2 June 2013 / Accepted: 5 August 2014 / Published: 25 August 2014

The powders of single-crystalline LiMn_2O_4 with different dimensional nanostructures were synthesized. The effect of nanostructure on the electrochemical properties of LiMn_2O_4 cathode was also investigated by controlling the nanostructure of LiMn_2O_4 , consisting of one-dimensional (1-D) nanorods with the diameter of 100 nm and length of 1.6 μm , of two-dimensional (2-D) nanoplates with the diameter ranging from 300 to 400 nm and a thickness of 20 nm, and of three-dimensional (3-D) octahedral single-crystals with edge length of 1 μm . It was found that the 1-D LiMn_2O_4 performed the best electrochemical properties with a high discharge capacity of 123.4 mAhg^{-1} , a stable cyclic retention, and an excellent rate capability (107.6 mAhg^{-1} at 10 C, 89.3% of 0.5 C-rate discharge capacity). Electrochemical impedance spectroscopy testing revealed the improved electrochemical performance, which could be considered that the nanostructure can reduce the impedance by enhancing the reaction area and lengthening the Li^+ diffusion length.

Keywords: Lithium manganese oxide; Nanomaterials; Dimension; Capacity retention; Rate performance.

1. INTRODUCTION

Lithium-ion batteries with high energy and power densities have received close attention for their wide applications on consumer electronic devices, portable powders tools, and new energy vehicles [1, 2]. Besides of the cell design, which is of great importance to its effect on the electrochemical performance, the electrode material is believed to be the most critical factor that affects the performance [3, 4]. Therefore, many researches have been done upon LiCoO_2 , LiFePO_4 ,

LiMn₂O₄ and Li₄Ti₅O₁₂, etc. [5-8]. Among them, LiMn₂O₄, with the three-dimensional (3-D) spinel structure as lithium pathway, has been spotlighted as a prospective candidate for the cathode material, due to its suitable Mn⁴⁺/Mn³⁺ redox potential (4V vs. Li⁺/Li), low-cost, environmental friendliness, and high abundance [6, 9, 10]. While, there are still some disadvantages of LiMn₂O₄, such as the significant capacity decay during cycling (especially at high temperatures of approximately 50°C), and poor performance under high ratio discharge (caused by Mn dissolution into the electrolyte, Jahn-Teller distortion, and lattice instability) [6, 11-13].

Nano-crystallization has been considered as a useful way not only to solve the above problems of LiMn₂O₄, but also to improve the performance of other electrode materials. This is achieved by the formation of large surface area to provide more reaction sites for Li and to shorten the Li⁺ diffusion length as shown in the equation: $L^2 = t \times D_{Li}$ (L: Li⁺ diffusion length, t: reaction time, D: mass diffusivity) [14-16]. Therefore, the researches on electrodes with nanostructures have attracted great interests. Baek et al. [17] prepared Li₂MnO₃ 2-D nano-plates by the hydrothermal treatment and analyzed the influence of phase transition for the improvement of electrode performance. Besides of 2-D nanostructure electrodes, many researches have been done on one-dimensional (1-D) materials, such as nanotubes, nanorods (LiCoO₂, LiNi_{0.8}Co_{0.2}O₂, Sn₂P₂O₇, V₂O₅, TiO₂, NaV₆O₁₅) [18-24] and nanofibers (K_{0.25}Mn₂O₄, Co₃O₄, TiO₂) [25-27], and zero-dimensional (0-D) materials, such as nanospheres and nanobeads (LiMn₂O₄, SnO₂, V₂O₅) [25-28] etc.

There were also some researchers reported the study on nanostructural LiMn₂O₄ for lithium-ion battery (see Table 1).

Table 1. Researches on the nanostructured lithium manganese oxide materials in lithium-ion battery reported.

Dimensions	Sample	Preparation method	Low-rate performance (mAhg ⁻¹)	High-rate performance (mAhg ⁻¹)
0-D	Li _{1.05} Mn ₂ O ₄ [25]	Solid-stated	1C-102	10C-85
	LiMn ₂ O ₄ [28]	Solid-stated	2C-105	10C-81.7
1-D	LiMn ₂ O ₄ [29]	Templated	0.1C-118	10C-102
	LiMn ₂ O ₄ [14]	Solid-stated	0.1C-112	/
	LiAl _{0.02} Mn _{1.98} O ₄ [36]	Solid-stated	0.1C-129.8	10C-110
	LiMn ₂ O ₄ [35]	Solid-stated	0.2C-130	7C-125
	LiMn ₂ O ₄ (this work)	Solid-stated	0.1C-123.4	10C-107.6
2-D	LiMn ₂ O ₄ [30]	Solid-stated	1C-100 (100% after 500 cycles)	8C-82
	LiMn ₂ O ₄ (this work)	Solid-stated	0.1C-122.7	10C-79.6

Luo et al. [25] prepared the LiMn₂O₄ hollow nanospheres through air-calcination of lithiated MnO₂ precursor, and analysis the influence of hollow spherical structure on the electrochemical performance. It was believed that the structure could provide not only a large surface area, but also thin wall which reduces the lithium-ion diffusion impedance. Kim et al. [14] detected two fundamental processes during the charge step of LiMn₂O₄ nanorods with a cubic phase, although the study was lack

of deep electrochemical performance analysis. Hosono [29] successfully synthesized LiMn_2O_4 nanowires with excellent rate performance based on a novel reaction method using $\text{Na}_{0.44}\text{Mn}_2\text{O}_4$ nanowires as a self-template. However, the process employed by Hosono was complicated, time-consuming, and hard to control, as it would take 4 days to form the $\text{Na}_{0.44}\text{Mn}_2\text{O}_4$ template. Sun et al. [30] prepared LiMn_2O_4 nanosheets through $\alpha\text{-MnO}_2$ coated with LiOH and analyzed the influence of exposed {111} facets for the improved electrode performance. The synthetic method of $\alpha\text{-MnO}_2$ nanosheets was also complicated and dynamically unstable.

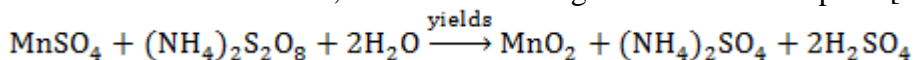
From the above review, there existed few reports on nanostructural LiMn_2O_4 single-crystal as synthesized through convenient methods with in-depth electrochemical property study. Few works have paid attention to the effect of dimension and surface area on nanostructural LiMn_2O_4 . In this work, we report a method to prepare 1-D, 2-D and 3-D LiMn_2O_4 materials and contrastively analyze the influence of nanostructure on the electrochemical properties at the level of an individual single crystalline particle. Further more, we for the first time report the new two-step method to synthesize the two dimensional LiMn_2O_4 nanoplates.

2. EXPERIMENTAL

2.1 Synthesis of 1-D, 2-D MnO_2 and corresponding LiMn_2O_4 powders

It is of great importance to control the syntheses of MnO_2 , as the nanostructured MnO_2 is the precursor which determines the morphology of LiMn_2O_4 . The synthesis procedure of LiMn_2O_4 nanorods and nanoplates includes two steps in this work: (1) preparation of nanostructured MnO_2 and (2) preparation of corresponding LiMn_2O_4 cathode material by the shape-controlled MnO_2 obtained from step (1). The MnO_2 nanorod and nanoplate precursors in this work were synthesized via a hydrothermal method.

In order to prepare the MnO_2 nanorods, 4.507 g $\text{MnSO}_4\cdot\text{H}_2\text{O}$ (supplied by Aldrich) was dissolved in distilled water under stirring for 30 min at room temperature, then 6.085 g $(\text{NH}_4)_2\text{S}_2\text{O}_8$ (also by Aldrich) was added into the solution under stirring for another 30 min at room temperature. The mixed solution was stilled in a 150 mL Teflon-lined stainless steel autoclave and annealed at 150 °C for 12 h. The obtained products were filtered and washed with distilled water for several times and then were dried at 80 °C for 12 h, after the following reaction was complete [31]:



The MnO_2 nanoplates were prepared as following: 5.27 g KMnO_4 (by Aldrich) was added to 100 mL distilled water under magnetic stirring at room temperature for 30 min to obtain atropurpureus solution. Then 0.76 g $(\text{NH}_4)_2\text{S}_2\text{O}_8$ (by Aldrich) and 0.56 g MnSO_4 (by Aldrich) were added to the solution. After being vigorously stirred for another 30 min, the solution was stilled in the 150 ml Teflon-lined stainless steel autoclave and then annealed at 100 °C for 72 h. The slurry formed was filtered and washed with distilled water at least 3 times and then dried in air at 80 °C for 12 h.

The corresponding nano LiMn_2O_4 powders were synthesized by the prepared MnO_2 . The mixture of 1.54 mmol $\text{LiOH}\cdot\text{H}_2\text{O}$ (by Aldrich) and 2.8 mmol MnO_2 was dissolved in absolute ethyl

alcohol under stirring for 5 h and then dried at room temperature. After repeated the above stirring and drying processes for another 2 times, the obtained products were further annealed at 700 °C for 10 h at the heating rate of 4 °C/min in oxygen atmosphere to yield nano- LiMn_2O_4 .

The final products were denoted 1-D LMO and 2-D LMO, respectively for LiMn_2O_4 synthesized from MnO_2 nanorods and nanoplates. The 3-D single-crystalline LiMn_2O_4 powders were also synthesized via a solid state method by annealing the well-ground mixture of stoichiometric Electrolytic Manganese Dioxide (EMD) and $\text{LiOH}\cdot\text{H}_2\text{O}$ at 450 °C for 12 h and then at 700 °C for 10 h in air. The blank sample was denoted 3-D LMO in this study.

2.2 Fabrication of nano- LiMn_2O_4 electrode

To fabricate the electrodes, a mixture of the prepared nano- LiMn_2O_4 powder (85 wt.%) as active material, acetylene black (10 wt.%) as conductive agent and polyvinylidene fluoride (PVDF, 5 wt.%) as binder was obtained. The above mixture was then dissolved in N-methyl-2-pyrrolidinone (NMP) solvent followed by stirring 4 h to yield uniform slurry. The slurry was finally coated on an aluminum foil acting as current collector and dried at 80 °C for 10 h.

2.3 Characterization

The phase composition of the synthesized powders were characterized by X-ray diffraction measurement (XRD, Rigaku D/max 2500/PC diffractometer (Rigaku Corp., Japan) using Cu $K\alpha$ radiation with $\lambda=1.5418 \text{ \AA}$). The specific surface area was measured by Brunauer-Emmet-Teller (BET) analysis. The morphology and microstructure were examined by a field emission scanning electron microscopy (FE-SEM, HITACH S4800, HITACH CO., Japan).

The electrochemical properties were measured on CR2032-type coin cells that were assembled in an argon filled glove box (Mbraum). The LiMn_2O_4 electrode was used as the cathode, and lithium metal foil was used as the anode. A $1 \text{ mol}\cdot\text{L}^{-1}$ of LiPF_6 in an ethylene carbonate-dimethyl carbonate (1:2 in volume, PANAX ETEC, Co., Ltd.) was used as the electrolyte with a polypropylene (Celgard 2500, Celgard Inc., USA) as separator. The charge-discharge cycles were performed at different current densities between 3.0 V and 4.3 V using a Land 2001A battery testing system at room temperature (RT). The electrochemical impedance spectroscopy (EIS) was performed using an electric IM6ex impedance analyzer over the frequency range of 10^{-3} to 10^6 Hz with an amplitude of 5 mV.

3. RESULTS AND DISCUSSION

3.1. Structural characterization and morphology of samples

According to Figures 1a and 1b, the X-ray diffraction patterns of MnO_2 nanorods and MnO_2 nanoplate obtained from hydrothermal reaction correspond respectively to JCPDS data No.65-2821 (β - MnO_2 , having tetragonal symmetry with $P4_2/mnm$ space group) and JCPDS data No.80-1098 (δ - MnO_2 ,

having monoclinic symmetry with C2/m space group) [32, 33]. SEM images in Figure 1c shows that the obtained β -MnO₂ consists of nanorods with an average diameter of about 50 nm and a length of 1 μ m to 2 μ m.

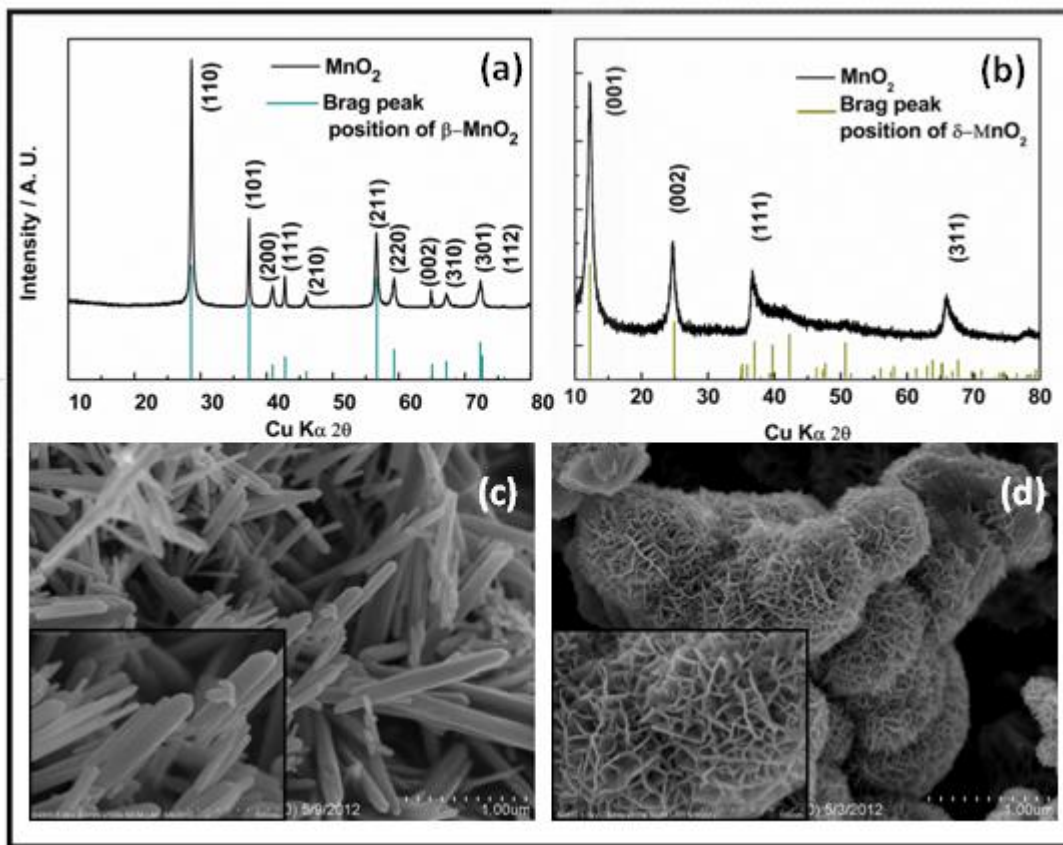


Figure 1. XRD patterns of (a) β -MnO₂ nanorods and (b) δ -MnO₂ nanoplates; FE-SEM images of (c) β -MnO₂ nanorods and (d) δ -MnO₂ nanoplates. **Error! Bookmark not defined.**

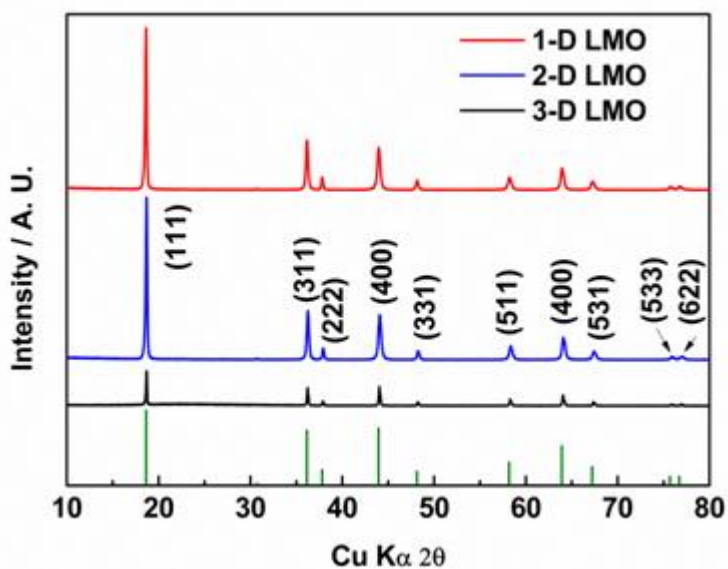


Figure 2. XRD patterns of 1-D LMO, 2-D LMO and 3-D LMO samples obtained.

It can be seen from Figure 1d that the obtained δ - MnO_2 consists of flower-like agglomerates made of nanoplates with the dimension ranging from 50 nm to 200 nm and a thickness less than 10 nm.

As indicated by Figure 2, all the peaks of LiMn_2O_4 samples are well matched to the Bragg-peak positions of LiMn_2O_4 (JCPDS card No. 35-0782) with cubic symmetry and $\text{Fd}3\text{m}$ space group. It is clearly that no additional impurity peaks or the β - MnO_2 , δ - MnO_2 , $\text{LiOH}\cdot\text{H}_2\text{O}$ phase are detected. Therefore, it is believed that the reaction between $\text{LiOH}\cdot\text{H}_2\text{O}$ and β - MnO_2 , δ - MnO_2 at 700 °C for 10 h is complete to produce pure LiMn_2O_4 .

In order to confirm the morphology of 1-D LMO, 2-D LMO, as well as 3-D LMO, the SEM images are shown in Figure 3.

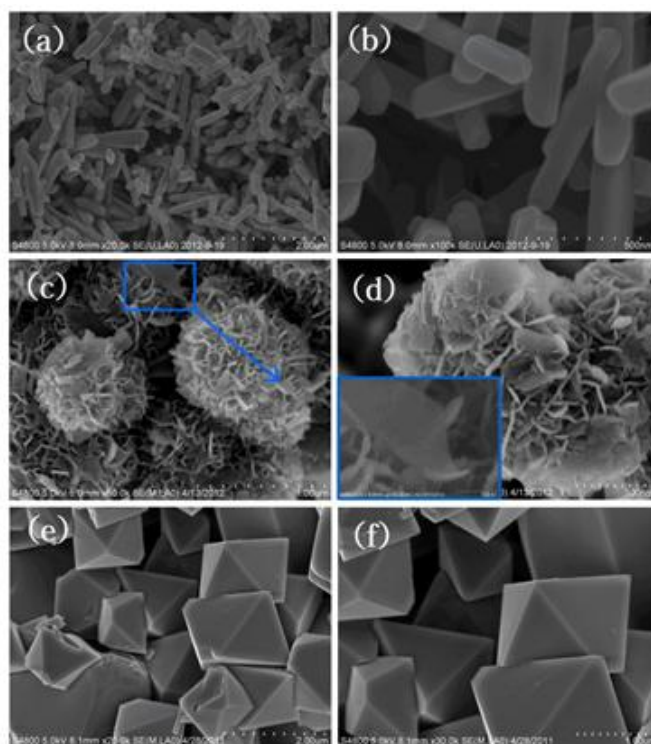


Figure 3. FE-SEM images of samples at different magnifications: (a) and (b) 1-D LMO, (c) and (d) 2-D LMO, (e) and (f) 3-D LMO single-crystalline samples .

It can be seen that the morphology remains intact after the 700 °C reaction for 1-D LMO and 2-D LMO samples. The 1-D LMO phase consists mainly of nanorods with an average diameter of 100 nm, which is larger than the prepared β - MnO_2 , and a length of about 1.6 μm (Figures 3a and 3b). Figures 3c and 3d show the FE-SEM images of 2-D LMO. The sample mainly contains nanoplates with diameter of 300 to 400 nm and a thickness of 20 nm, which is thicker than the thickness of sample in Ref. [30]. This could be due to the different reaction conditions (annealed at 700 °C for 4 h in Ref. [30], but at 700 °C for 10 h in this work). On the other hand, the morphology of 3-D LMO sample (Figs. 3e and 3f) shows significantly octahedral single-crystalline particles with edge length of about 1 μm.

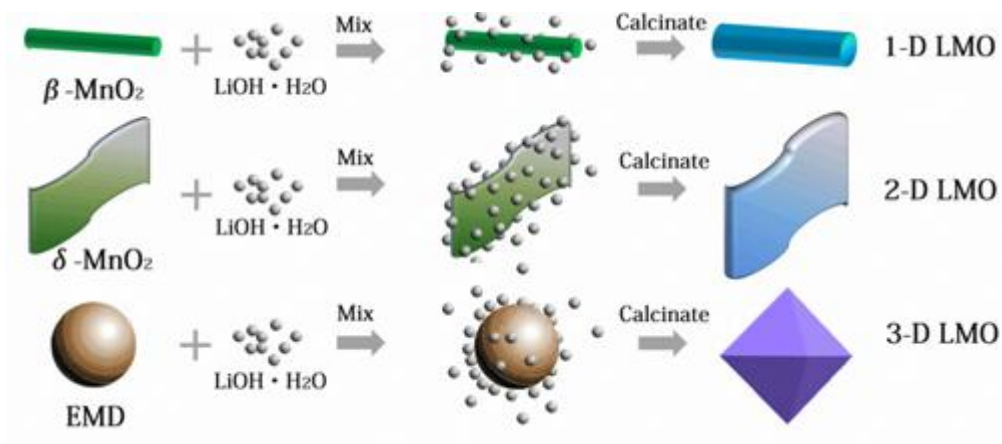


Figure 4. Scheme of the formation mechanism of 1-D, 2-D and 3-D LiMn_2O_4 single-crystalline samples.

As schematically represented in Figure 4, after the reaction, the 1-D, 2-D LMO samples retain the stick-like and plate-like morphologies, respectively, as those of the prepared $\beta\text{-MnO}_2$ and $\delta\text{-MnO}_2$, while the 3-D LMO sample based on EMD precursor changed from a spherical-shape particle to an octahedral-shape particle.

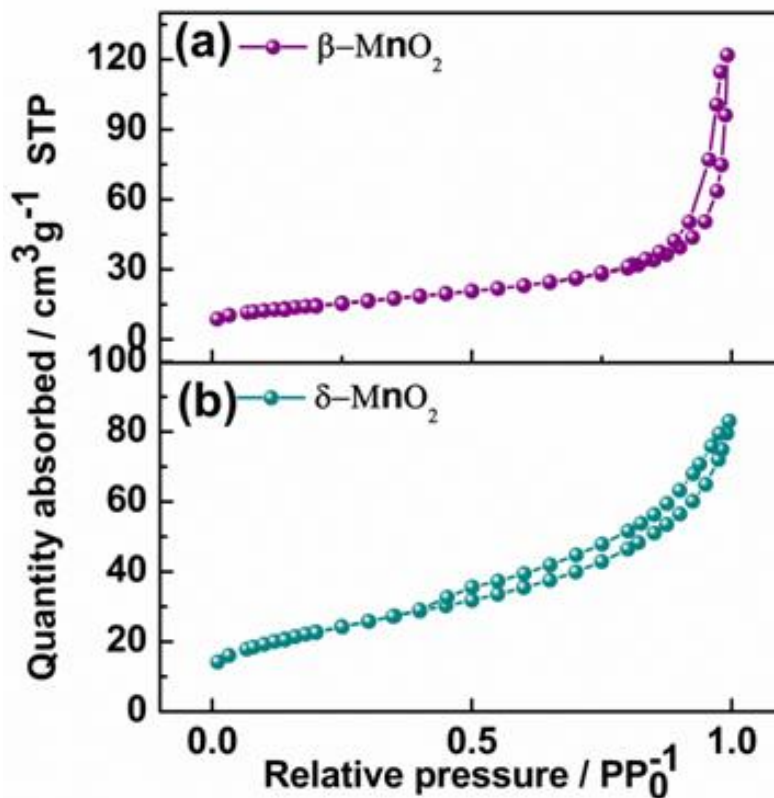


Figure 5. N_2 adsorption-desorption isotherms of (a) $\beta\text{-MnO}_2$ and (b) $\delta\text{-MnO}_2$.

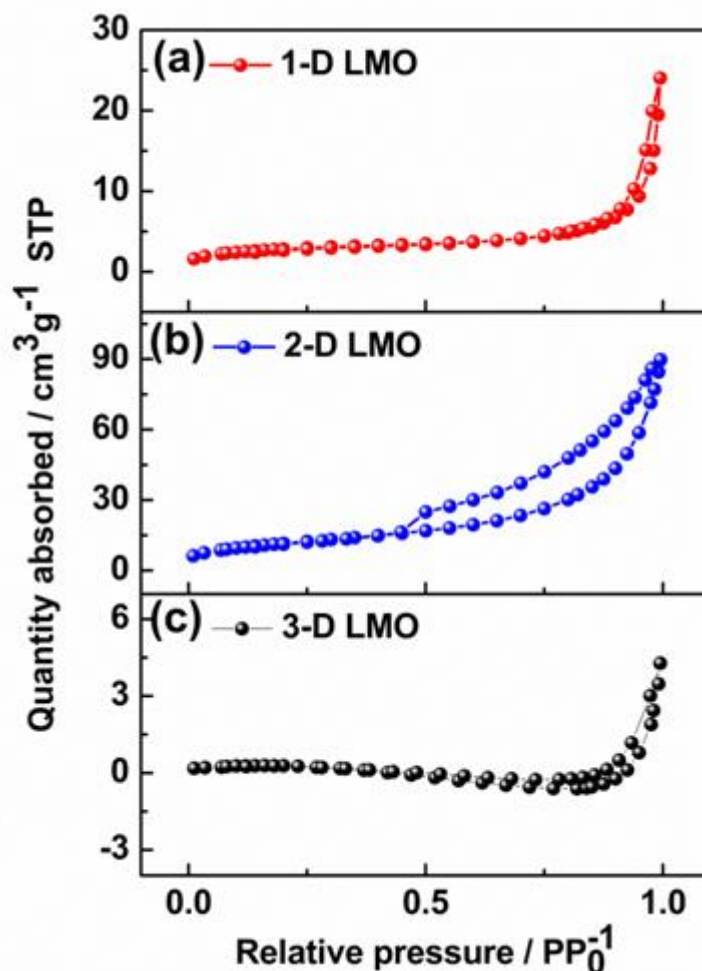


Figure 6. N_2 adsorption-desorption isotherms of (a) 1-D LMO, (b) 2-D LMO and (c) 3-D LMO.

To verify the relationship between the numbers of reaction areas for Li, N_2 adsorption isotherms distributions of the prepared β - MnO_2 , δ - MnO_2 , 1-D LMO, 2-D LMO and 3-D LMO were measured by Brunauer-Emmet-Teller (BET) analysis, and the results are shown in Figure 5 and Figure 6. According to the IUPAC classification, all the curves correspond to type II, displaying a small hysteresis loop, which are traditionally attributed to meso-porous solids with some contribution by micropores [34]. The predominant adsorption uptakes of β - MnO_2 , 1-D LMO and 3-D LMO are above $P/P_0=0.8$, indicating a larger average pore size of the prepared $LiMn_2O_4$. According to the BET results, the BET specific surface area of the β - MnO_2 ($52.91 \text{ m}^2\text{g}^{-1}$) is higher than that of 1-D LMO ($10.30 \text{ m}^2\text{g}^{-1}$), which is similar with $LiMn_2O_4$ nanorod samples in Refs. [35] and [36], because of the particle growth during the annealing reaction. The 2-D LMO sample has the largest surface area ($52.91 \text{ m}^2\text{g}^{-1}$) among all $LiMn_2O_4$ samples, while that of 3-D LMO sample is very small ($1.01 \text{ m}^2\text{g}^{-1}$).

3.2. Electrochemical test

The cyclic performances of the 1-D, 2-D and 3-D LMOs were tested with an aggressive test profile using a voltage window of 3.0~4.3 V and a current density of 0.1 C at room temperature

(Figure 7). The 1-D LMO delivers a discharge capacity of 123.4 mAhg^{-1} at the beginning. The capacity retention (retention=ratio of discharge capacity at the 100th cycle to that at the 1st cycle) of the 1-D LMO electrodes (81.3 %) is superior to that of the 2-D LMO (76.9 %) and 3-D LMO electrodes (51.8 %) after 100 cycles.

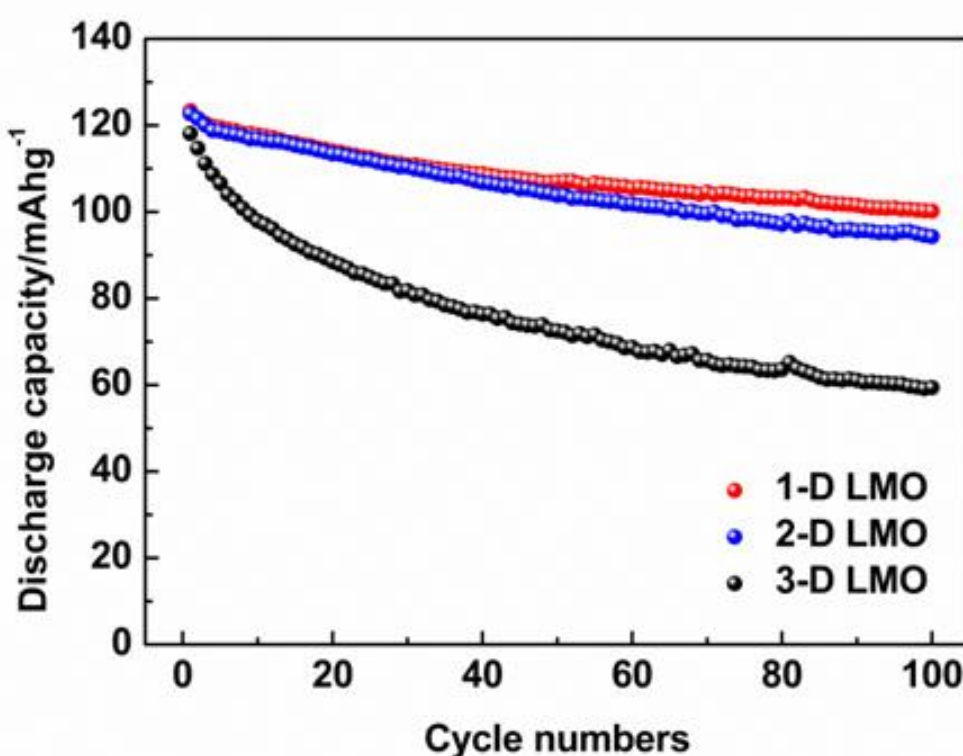


Figure 7. The cycle ability of 1-D, 2D and 3-D-LMO samples at a current density of 0.1 C-rate (at room temperature).

As shown in Figures 8a, 8b and 8c, all the cells made by the obtained LiMn_2O_4 exhibit two voltage plateaus. These two plateaus are related to two steps when the LiMn_2O_4 electrodes discharge. The first one corresponds to an extraction of Li-ions from half of the tetrahedral sites with Li-Li interaction, and the second one to an extraction of Li ions from the other half of the tetrahedral sites without Li-Li interaction [13, 37]. It also can be found that the plateau width decreased sharply with cycling for the 3-D LMO after 100 cycles, while the voltage profiles at the 100th cycle are fairly close to the first cycle for the 1-D LMO electrode. Figure 8d, 8e and 8f show differential capacity-voltage dQ/dV plots for the 1st, 25th, 50th, 75th and 100th cycles. All the prepared LiMn_2O_4 exhibited two distinct peaks which correspond to the flat plateau shown in Figures 8a, 8b and 8c. The further cycling caused the peaks shift farther apart for 3-D LMO electrodes, while that for 1-D LMO electrodes remained almost unchanged except for the first cycle. The results suggest that the 1-D LMO could suppress the structural change induced by phase transition during cycling.

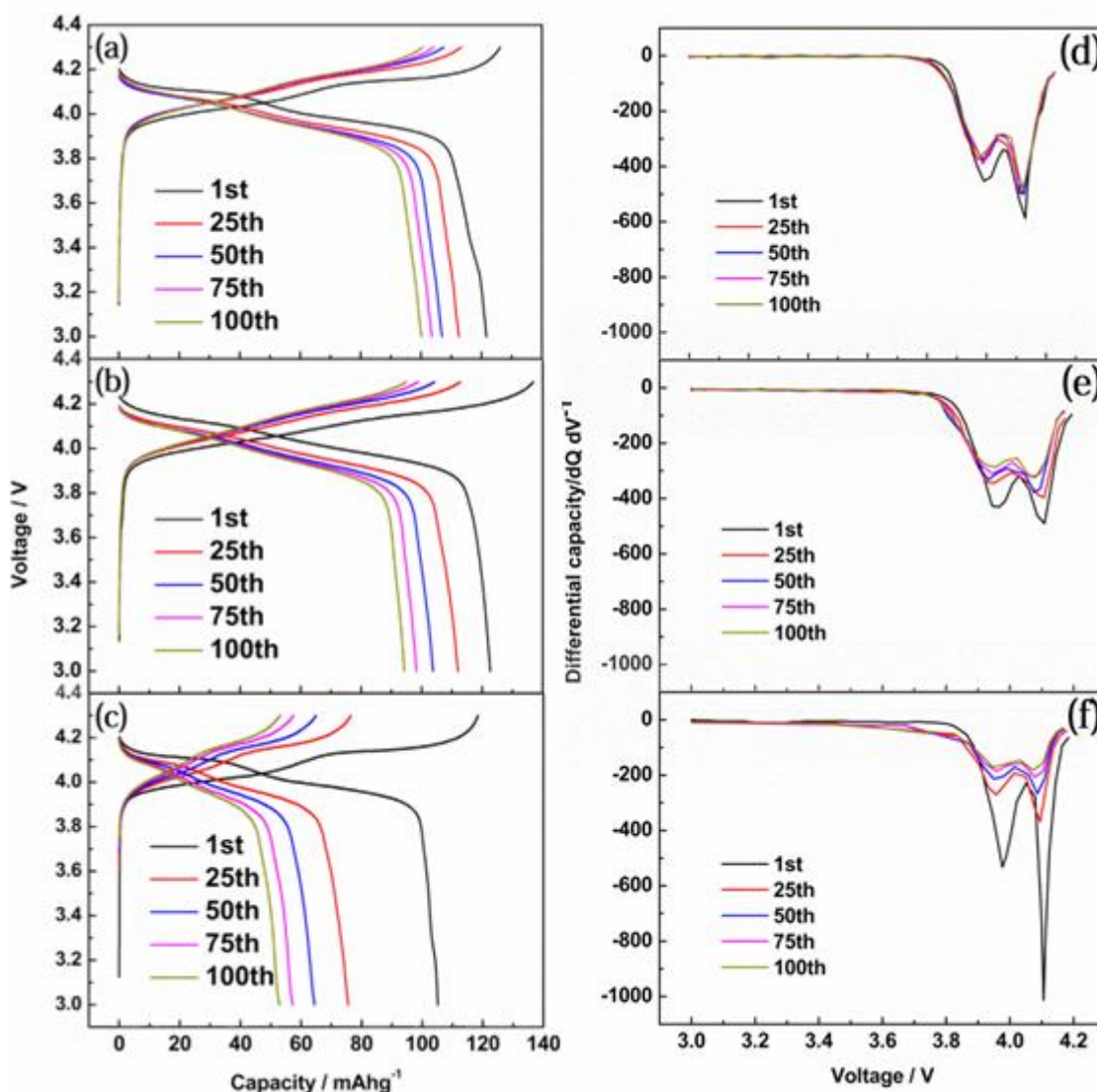


Figure 8. Continuous charge and discharge curves of (a) 1-D LMO, (b) 2-D LMO, and (c) 3-D LMO cells; the differentiated curves for discharge of (d) 1-D LMO, (e) 2-LMO and (f) 3-D LMO cells.

Figure 9d shows rate capabilities of samples at different discharge rates from 0.5 C to 10 C at room temperature. The first charge and discharge capacities of the 3-D LMO are 120.1 and 109.9 mAhg^{-1} , showing a coulombic efficiency of 92 %, while those of the 1-D LMO and 2-D LMO are 125.8, 120.5 mAhg^{-1} , 96 %, and 125.8, 119.9 mAhg^{-1} , 95.3 %, respectively. The discharge capacities of the 3-D LMO decreases as 92.9, 82.8, 69.8 and 60.9 mAhg^{-1} when the current rate increases to 1, 2, 5 and 10 C. On the other hand, the discharge capacities are 116.5, 116.4, 112.4, and 104.6 mAhg^{-1} for 1-D LMO corresponding to 1, 2, 5 and 10 C, and 119.9, 116.2, 111.4, 96.8, and 79.6 mAhg^{-1} for the 2-D LMO, at the same current rate as the 3-D LMO sample (Figures 9a, 9b and 9c). The results indicate that the 1-D LMO have a best rate property, which is correlated to the appropriate BET surface area.

To delineate the structural degradation with interfacial impedance at the interface between the cathode electrodes and the electrolyte, electrochemical impedance spectroscopy (EIS) was performed on the 1-D, 2-D and 3-D LMO electrodes after fully being charged to 4.3 V (vs. Li/Li^+), as shown in

Figure 10. Z-view software was used to simulate the EIS data using the equivalent circuit (Figure 10a), in which, R_b referred to a bulk resistance including the resistances of the electrolyte, electrode substrate metal, electrode leads, terminals, etc., R_{ct} referred to the charge-transfer resistance, CEP1 refers to the corresponding constant-phase element, and Z_w referred to the Warburg impedance related to the solid-state diffusion of lithium ion within the active materials.

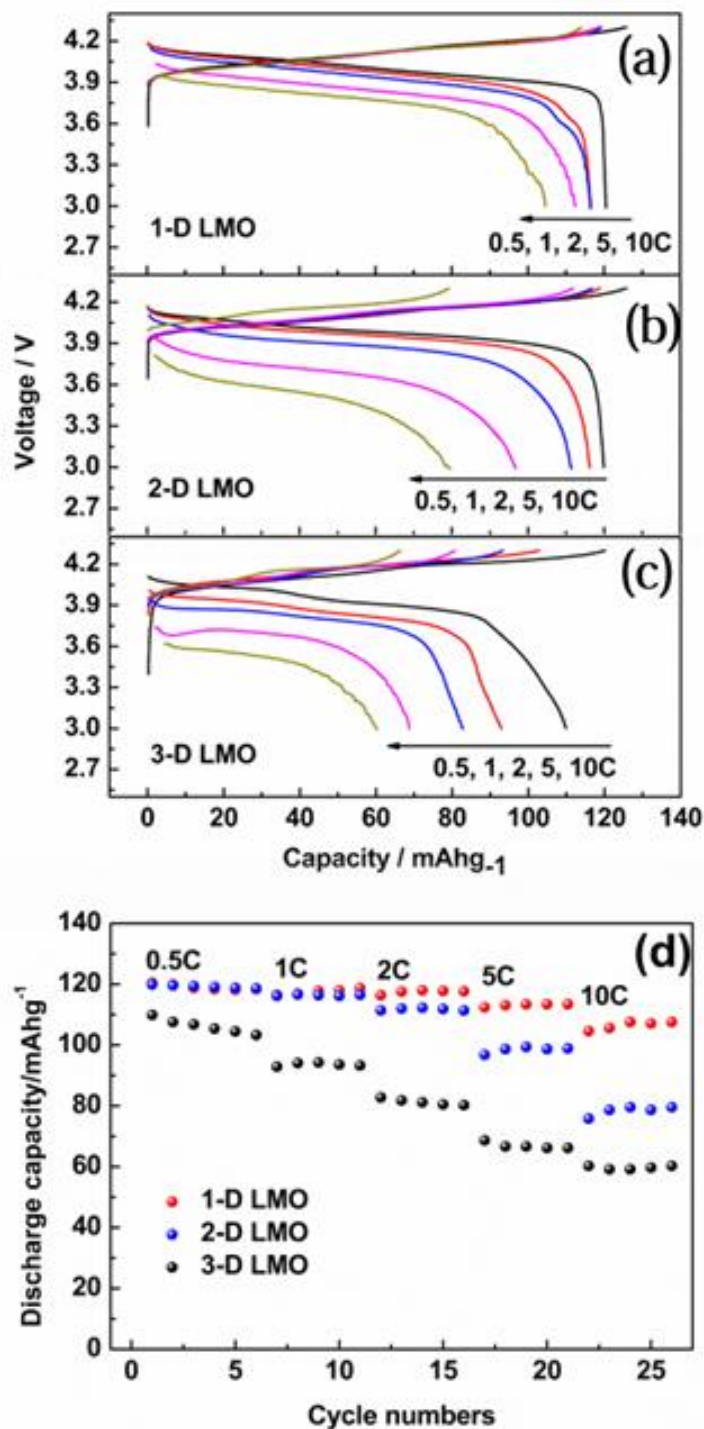


Figure 9. Voltage profiles of (a) 1-D LMO, (b) 2-D LMO and (c) 3-D LMO electrodes at different C rates; (d) Rate capability of 1-D LMO, 2-D LMO and 3-D LMO electrodes at different C rates between 3 and 4.3 V of coin-type half cells (at room temperature).

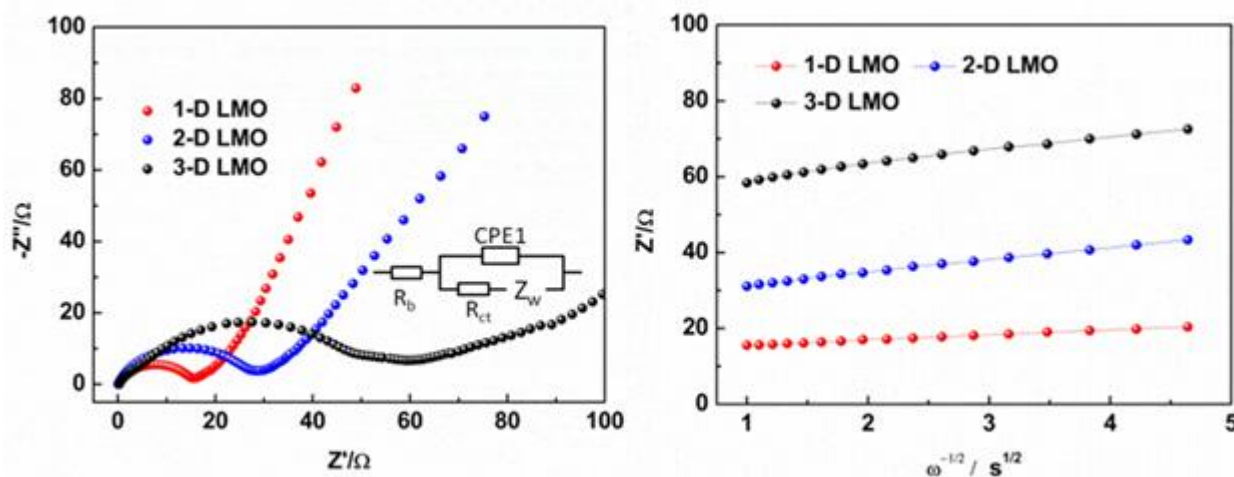


Figure 10. (a) EIS profiles of the 1-D LMO, 2-D LMO and 3-D LMO; (b) corresponding real parts of the complex impedance versus $\omega^{-1/2}$ at LiMn_2O_4 50% SOC.

It can be seen that each of the Nyquist plots includes two parts: one high to medium semicircle corresponding to the R_{ct} and CPE1, one low –frequency sloping line corresponding to the Z_w .

Table 2. Simulation result of Figure10

Samples	R_b/Ω	R_{ct}/Ω	σ	$D_{Li}/\text{cm}^2\text{s}^{-1}$
1-D LMO	2.82	13.61	1.53	4.36×10^{-11}
2-D LMO	2.37	27.95	3.73	7.38×10^{-12}
3-D LMO	1.43	42.44	5.19	3.81×10^{-12}

The simulation results given in Table 2 show that the R_b of the 1-D LMO and 2-D LMO are 2.82 Ω and 2.37 Ω , which are larger than that of 3-D LMO (1.43 Ω). This suggests that the nano 1-D and 2-D structures are beneficial for increasing the electronic conductivity of particles, whereas the R_{ct} of 1-D LMO (13.61 Ω) and 2-D LMO (27.95 Ω) are much less than that of 3-D LMO (42.44 Ω). It suggests that 1-D and 2-D LMO have larger Li ion conductivity, which can be further confirmed by following calculation according to equation (1) [38, 39] :

$$D_{Li} = \frac{R^2 T^2}{2A^2 n^4 F^4 C^2 \sigma^2} \tag{1}$$

where D_{Li} is the mass diffusivity of the Li^+ ; R is the gas constant; T is the absolute temperature; A is the electrode area; n counts the number of electrons per molecule during oxidization; F is the Faraday constant (96485 Coulomb/mol); C is the concentration of the Li^+ ; and σ is the Warburg coefficient. In this case, the σ value could be obtained from the lines as shown in Figure10 b according to equation (2):

$$Z' = R_{ct} + \sigma \omega^{-1/2} \tag{2}$$

The results of D_{Li} for the test samples as calculated using equation (1) are shown in Table 2. All the D_{Li} of samples are within the range from 10^{-10} to $10^{-13} \text{ cm}^2\text{s}^{-1}$, which is fit to the general rules of

LiMn_2O_4 cathode material. It is clearly shown that the D_{Li} of the 1-D LMO ($4.36 \times 10^{-11} \text{ cm}^2 \text{ s}^{-1}$) is about 12 times higher than that of the 3-D LMO ($3.81 \times 10^{-12} \text{ cm}^2 \text{ s}^{-1}$). It can be speculated that the 1-D and 2-D LMO could provide longer Li^+ diffusion length, which would improve the electronic conductivity of the electrodes (Fig.11). The appropriately larger surface has more available sites for Li-ion insertion and extraction, especially at high charge-discharge rates. When the surface area is too large, the reaction between the HF-contained electrolyte and LiMn_2O_4 electrodes would be aggravated, which leads to severe Mn dissolution and structure instability during charge and discharge steps. Therefore the electrochemical performance of 2-D LMO is not as good as that of 1-D LMO, which can be confirmed from the results shown in Figure 10.

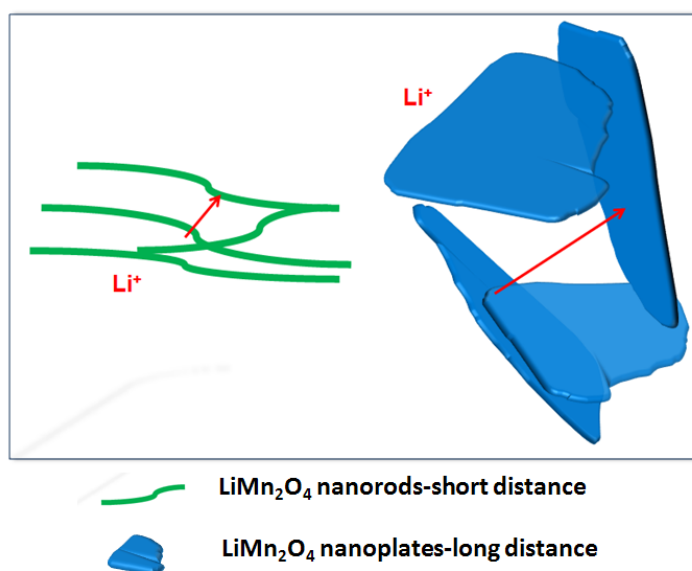


Figure 11. Scheme of the Li^+ diffusion length for LiMn_2O_4 nanorods and LiMn_2O_4 nanoplates samples.

4. CONCLUSIONS

Single-crystalline 1-D, 2-D and 3-D LiMn_2O_4 powders were successfully synthesized, using $\beta\text{-MnO}_2$ nanorods, $\delta\text{-MnO}_2$ nanoplates (prepared by the hydrothermal method), and EMD as precursors, respectively. The nanostructural effect of the LiMn_2O_4 cathode on the electrochemical performance was explored. XRD data and SEM images confirmed that the LiMn_2O_4 nanorods were well formed with the average diameter of 100 nm, and length of about 1.6 μm , so as the LiMn_2O_4 nanoplates with dimension of 300 to 400 nm and thickness of 20 nm, and the LiMn_2O_4 octahedral single-crystal with edge length of about 1 μm . The correlation among the nanostructured electrodes, made of the 1-D, 2-D and 3-D LiMn_2O_4 powders, and their kinetic properties was also examined from a comparison of the surface area of the samples. The electrodes, made of the 1-D LiMn_2O_4 nanorods and 2-D nanoplates synthesized by hydrothermal method, showed improved electrochemical performances such as cyclic performance and rate-capability as compared with that of the 3-D LiMn_2O_4 synthesized through a solid-state method. After 100 cycles the capacity remained 81.3 % of the initial value (123.4 mAhg^{-1}) for the 1-D LiMn_2O_4 nanorods electrode, and 76.9 % for the 2-D LiMn_2O_4 nanoplates

electrode, while that of the 3-D LiMn_2O_4 electrode was 51.8 %. The enhanced reaction area and lengthened Li^+ diffusion length were believed to be responsible for the improvement of the electrode performance of nano LiMn_2O_4 electrodes. However, when the surface area is too large, the aggravated reaction between HF-contained electrolyte and electrodes would be adverse to the electrochemical performance.

ACKNOWLEDGEMENTS

This work was financially supported by the Natural Science Foundation of China under Grants Nos.51072131, 51202121 and 51232005, Shenzhen Projects for Basic Research, Guangdong Province Innovation R&D Team Plan for Energy and Environmental Materials (No.2009010025).

References

1. R.J. Martin Winter, Brodd, *Chem.Rev.*, , 104 (2004) 4245-4267.
2. J.G. Bruno Scrosati, *J. Power Sources*, 195 (2010) 2419-2430.
3. S.P. Min-Kyu Song, Faisal M.Alamgir, Jaephil Cho, Meilin Liu, *Mater. Sci. Eng. R-Rep*, 72 (2011) 203-252.
4. D.Q. Bo Xu, Ziyang Wang, Ying Shirley Meng, *Mater. Sci. Eng. R-Rep*, 73 (2012) 51-65.
5. S. Valanarasu, R. Chandramohan, R.M. Somasundaram, S.R. Srikumar, *J. Mater Sci-Mater El* , 22 (2011) 151-157.
6. J.M. Tarascon, E. Wang, F.K. Shokoohi, W.R. McKinnon, S. Colson, *J. Electrochem. Soc*, 138 (1991) 2859-2864.
7. P. Barboux, J.M. Tarascon, F.K. Shokoohi, *J. Solid State Chem*, 94 (1991) 185-196.
8. B. H. LI, C. P. Han, Y. B. He, C. Yang, H. Du, Q. H. Yang, F. Y. Kang, *Energ Environ. Sci.* 5(2012) 9595-9602.
9. L.L. Xiong, Y.L. Xu, C. Zhang, Z.W. Zhang, J.B. Li, *J. Solid State Electrochem.*, 15 (2011) 1263-1269.
10. C.Y. Wan, M. Cheng, D. Wu, *Powder Technol*, 210 (2011) 47-51.
11. M.T. Atsuo Yamada, Koichi Tanaka, Koji Sekai, *J. Power Sources*, 81-82 (1999) 73-78.
12. J.M. Tarascon, W.R. McKinnon, F. Coowar, T.N. Bowmer, G. Amatucci, D. Guyomard, *J. Electrochem. Soc*, 141 (1994) 1421-1431.
13. T. Ohzuku, M. Kitagawa, T. Hirai, *J. Electrochem. Soc*, 137 (1990) 769-775.
14. D.K. Kim, P. Muralidharan, H.W. Lee, R. Ruffo, Y. Yang, C.K. Chan, H. Peng, R.A. Huggins, Y. Cui, *Nano Lett*, 8 (2008) 3948-3952.
15. M. Okubo, Y. Mizuno, H. Yamada, J. Kim, E. Hosono, H. Zhou, T. Kudo, I. Honma, *Acs Nano*, 4 (2010) 741-752.
16. H. Xia, Z. Luo, J. Xie, *PNSMI*, 22 (2012) 572-584.
17. J.Y. Baek, H.W. Ha, I.Y. Kim, S.J. Hwang, *J. Phys. Chem. C*, 113 (2009) 17392-17398.
18. X.X. Li, F.Y. Cheng, B. Guo, J. Chen, *J. Phys. Chem. B*, 109 (2005) 14017-14024.
19. P. Liu, S.H. Lee, C.E. Tracy, Y.F. Yan, J.A. Turner, *Adv. Mater.*, 14 (2002) 27-30.
20. I. Moriguchi, R. Hidaka, H. Yamada, T. Kudo, H. Murakami, N. Nakashima, *Adv. Mater.*, 18 (2006) 69-73.
21. A.R. Armstrong, G. Armstrong, J. Canales, P.G. Bruce, *Angew. Chem.-Int. Edit*, 43 (2004) 2286-2288.
22. E. Kim, D. Son, T.G. Kim, J. Cho, B. Park, K.S. Ryu, S.H. Chang, *Angew. Chem.-Int. Edit*, 43 (2004) 5987-5990.
23. H.S. Zhou, D.L. Li, M. Hibino, I. Honma, *Angew. Chem.-Int. Edit*, 44 (2005) 797-802.

24. H.M. Liu, Y.G. Wang, L. Li, K.X. Wang, E. Hosono, H.S. Zhou, *J. Mater Chem*, 19 (2009) 7885-7891.
25. L.C. Jiayan Luo, Yongyao Xia, *Electrochem Commun*, 9 (2007) 1404-1409.
26. A.M. Cao, J.S. Hu, H.P. Liang, L.J. Wan, *Angew. Chem.-Int. Edit*, 44 (2005) 4391-4395.
27. H. Sangjin, J. Byungchul, K. Taeahn, S.M. Oh, H. Taeghwan, *Adv Funct Mater*, 15 (2005) 1845-1850.
28. W. Tang, X.J. Wang, Y.Y. Hou, L.L. Li, H. Sun, Y.S. Zhu, Y. Bai, Y.P. Wu, K. Zhu, T. van Ree, *J. Power Sources*, 198 (2012) 308-311.
29. T.K. Eiji Hosono, Itaru Honma, Hirofumi Matsuda, Haoshen Zhou, *Nano Lett*, 9 (2008) 1045-1051.
30. W. Sun, F. Cao, Y. Liu, X. Zhao, X. Liu, J. Yuan, *J. Mater Chem*, 22 (2012) 20952-20957.
31. X. Wang, Y.D. Li, *J. Am Chem Soc*, 124 (2002) 2880-2881.
32. X.D. Liu, C.Z. Chen, Y.Y. Zhao, B. Jia, *J. Nanomater*, (2013) 36375-36375.
33. X. Wang, Y.D. Li, *Chem-Eur J*, 9 (2003) 300-306.
34. G. Aranovich, M. Donohue, *J. Colloid Interf Sci*, 200 (1998) 273-290.
35. J. Cho, *J. Mater Chem*, 18 (2008) 2257-2261.
36. W.-H. Ryu, J.-Y. Eom, R.-Z. Yin, D.-W. Han, W.-K. Kim, H.-S. Kwon, *J. Mater Chem*, 21 (2011) 15337-15342.
37. M.M. Thackeray, W.I.F. David, P.G. Bruce, J.B. Goodenough, *Mater Res Bull*, 18 (1983) 461-472.
38. A.S. Norio Takami, Michikazu Hara, Takahisa Ohsaki, *J. Electrochem. Soc.*, 142 (1995) 371-379.
39. S. Rodrigues, N. Munichandraiah, A.K. Shukla, *J. Power Sources*, 87 (2000) 12-20